Environmental Science Nano

ROYAL SOCIETY OF CHEMISTRY

PAPER

View Article Online
View Journal | View Issue

Cite this: *Environ. Sci.: Nano*, 2024, **11**, 1682

Influence of time and ageing conditions on the properties of ferrihydrite†

Michel Sassi, [a] Odeta Qafoku, [b] Mark E. Bowden, [b] Carolyn I. Pearce, [a] Drew Latta, [c] Quin R. S. Miller, [a] Mavis D. Boamah, [a] Alpha T. N'Diaye, [d] Jade E. Holliman Jr., [a] Elke Arenholz [a] and Kevin M. Rosso *[a]

Natural conversion of ferrihydrite (Fh), a widespread Fe(III)-oxyhydroxide mineral at the Earth's surface, to thermodynamically more stable iron oxides such as goethite (Gt) and hematite (Hm) is a slow process that spans months to years. Here we examined the effects of synthesis and storage conditions on the hydration, the ratio of tetrahedral to octahedral iron sites, and the transformation of naturally aged 2-line Fh at room temperature and mildly acidic pH over an ageing period of 5 years. Fh samples synthesized and aged in either aerobic or anaerobic conditions were characterized over time by XRD, SEM, thermogravimetric analysis – mass spectroscopy (TGA-MS), and X-ray absorption spectroscopies (XANES and XMCD). The findings show that the ratio of tetrahedral to octahedral Fe(III) sites in Fh is correlated to its extent of hydration, with fresher Fh samples exhibiting a higher ratio and more bound water. Fresh Fh aged in aerobic conditions has similar bound inorganic carbon, is more hydrated, and has less tetrahedral Fe(III) than that aged in anaerobic conditions. Hence, for relatively fresh Fh there is a link between Fh properties and storage conditions. However, the long-term ageing characteristics, such as the transformation rate and relative phase fraction of Gt and Hm products, are not noticeably impacted by storage conditions. TGA-MS measurements coupled with O K-edge XANES spectra confirm that Fh tends to lose its hydration as it ages, as expected. Corresponding Fe $L_{2,3}$-edge XMCD spectra reveal that this dehydration is coupled to a steady decrease in the ratio of tetrahedral to octahedral Fe(III) sites. In addition to the obvious constraints these findings place on making comparisons across Fh samples of different age and environmental settings, they also highlight that Fh structure, and consequently magnetism, are linked to its bound water content.

Received 14th November 2023,
Accepted 22nd February 2024

DOI: 10.1039/d3en00828b

rsc.li/es-nano

Environmental significance

Ferrihydrite is a metastable iron-oxyhydroxide nanomineral, ubiquitous in surface environments, and crucial in environmental geochemistry. With reactive hydroxyl groups being important drivers for catalytic reactions on mineral nanoparticles, ferrihydrite has great potential for the capture of contaminants in natural and industrial waters. Long studied, its structure and composition remain elusive, and a consensus, especially regarding its hydration and tetrahedral iron content, has yet been reached. This study shows that tetrahedral iron and hydroxyl populations of fresh ferrihydrite are correlated. While their initial populations are affected by the ageing conditions, both populations decrease over time. This suggests an evolution in the surface reactive properties of ferrihydrite as a function of its age and ageing conditions.

1. Introduction

Since its discovery in the 1970's,[1] ferrihydrite (Fh) has been the focus of active research because of its widespread presence at the Earth's surface in soils and aquatic environments where it can act as a strong sorbent with high sorption capacity.[2] These characteristics have also led to its use in industry as a cost-effective sorbent.[3,4] Fh is a poorly crystalline iron-oxyhydroxide nanomineral which exists exclusively as spherical nanoparticles with sizes typically ranging from 2 to 10 nm.[5] Because its precise structure is

[a] *Pacific Northwest National Laboratory, Richland, WA 99352, USA. E-mail: Kevin.Rosso@pnnl.gov*
[b] *Environmental Molecular Sciences Laboratory, Pacific Northwest National Laboratory, Richland, WA 99352, USA*
[c] *Department of Civil and Environmental Engineering, University of Iowa, Iowa City, Iowa 52242, USA*
[d] *Advanced Light Source, Lawrence Berkeley National Laboratory, Berkeley, California 94720, USA*

† Electronic supplementary information (ESI) available. See DOI: https://doi.org/10.1039/d3en00828b

difficult to determine unambiguously using X-ray diffraction (XRD) and scattering techniques, the extent of structural ordering in Fh is distinguished based on the number of peaks present in the XRD pattern; so-called 2- and 6-line Fh are the most common types observed.[2,6,7] While X-ray pair distribution function (PDF) analysis suggest that these structures are similar,[8] the main difference between 2- and 6-line Fh is essentially due to the variation in the average size of the coherent scattering domains. This is consistent with observations that 2-line Fh generally has smaller particle sizes, ranging from 1 to 4 nm, and is more hydrated, than 6-line Fh.[5,8–13]

For several decades, precise determination of the structure and composition of Fh has been the focus of intense debate and is still not fully resolved. Several models[2,14] from single-phase[15,16] to multi-[17,18] and hybrid-phase[19] have been proposed, spanning a range of hydration encompassed by the approximate chemical formula of $Fe_5O_8H + nH_2O$.[2,17,18,20,21] Recent theoretical studies offered a new perspective in which Fh, especially 2-line Fh, could be viewed as a nanocomposite of distinct coexisting structure types indistinguishable by X-ray scattering whose distribution at any given time depends on factors such as particle size, temperature, and the activity of water.[17,22] Another important aspect of the structure of Fh is the extent to which tetrahedral Fe sites are intrinsic. In this regard, Mössbauer spectroscopy[23] does not indicate tetrahedral Fe,[24,25] while X-ray based spectroscopies such as X-ray absorption near edge structure (XANES) and X-ray magnetic circular dichroism (XMCD) do indicate tetrahedral Fe.[26–28] Studies that provide evidence for tetrahedral sites in Fh tend to estimate this Fe site fraction in the range of 20–30%.[15,27] Uncertainties on the hydration and tetrahedral Fe content are in part due to the difficulty of distinguishing bulk *versus* surface contributions.[29,30]

Because Fh is metastable with respect to more crystalline iron-(oxyhydr)oxides such as goethite (Gt) and hematite (Hm), it transforms over time.[31–33] Although various transformation mechanisms have been proposed, including solid-state recrystallization[31] potentially mediated by particle aggregation,[34] dissolution–reprecipitation appears to be the most likely pathway.[31,35,36] Because of the low aqueous solubility of Fe(III) at circumneutral pH, this spontaneous transformation of Fh to Gt/Hm can take years.[31,37] In contrast, redox-catalysis enables transformation in a matter of hours,[38,39] by increasing the lability and effective mass flux of Fe(III).[40–43] In the absence of redox-catalysis, the slow and spontaneous transformation of Fh to Gt/Hm is known to depend on at least temperature and pH.[31,37,44] Several experimental investigations have also demonstrated the ability of silicate,[45–47] arsenate,[48] and phosphate[49] to inhibit Fh dissolution and transformation to Gt, nominally because these oxyanions strongly adsorb as inner-sphere complexes on the Fh surface.

However, although Fh transformation has been well studied in various contexts, to our knowledge there has yet to be a systematic investigation of the unresolved questions pertaining to the structure and composition of Fh over time at a given set of conditions. Specifically, are there detectable linkages between Fh structural characteristics (*e.g.*, tetrahedral Fe content) and its composition (*e.g.*, extent of hydration) over time and if so why? And how sensitive are any such linkages to synthesis or storage conditions? Answering these questions could provide insight into the structure of Fh itself, and factors that govern its formation and stability in the environment.

Here we investigated the effects of synthesis and storage conditions on the evolution of 2-line Fh over time at room temperature at mildly acidic pH, monitoring its structural and hydration properties throughout ageing from initial synthesis up until 5 years duration. Although during ageing Fh gradually becomes an assemblage of Fh/Gt/Hm, our study was designed to focus on the Fh fraction. In addition to X-ray diffraction (XRD) and scanning electron microscopy (SEM), isolation of the Fh fraction is enabled in part by use of X-ray absorption spectroscopies. In particular, Fe L-edge X-ray circular magnetic dichroism (XMCD) spectroscopy is sensitive only to the magnetically ordered Fe fraction of a magnetic material.[50,51] In the phase assemblage Fh/Gt/Hm, only Fh is expected to bear a net magnetic moment,[52–54] particularly at low temperature.[55,56] Hence the measured Fe-L edge XMCD signal arises largely from iron associated with Fh. Other techniques used such as thermogravimetric analysis – mass spectroscopy (TGA-MS) isolates the hydration properties associated with the Fh fraction by separation from known thermal dehydration thresholds of other phases that bear structural water such as Gt.[57] We compare time-dependent Fh characteristics when synthesized aerobically and stored either aerobically or anaerobically. Questions pertaining to the possible role of dissolved inorganic carbon are investigated by comparing aerobically *versus* anaerobically synthesized Fh during early stages of ageing with or without air exposure. All cases examined show only small initial differences that converge after several weeks. We show that freshly precipitated 2-line Fh has a relatively large tetrahedral Fe fraction that diminishes as Fh ages, and that this is coupled to a progressive decrease in its structural water content. For fresh Fh samples, aerobic/anaerobic storage conditions are found to more strongly affect the tetrahedral Fe content than aerobic/anaerobic synthesis conditions. However, the storage conditions don't noticeably impact the long-term transformation rate and end-product ratio.

2. Materials and methods

2.1 Ferrihydrite synthesis

Synthesis of the Fh was based on procedure described by Qafoku *et al.*[35] In detail, 5 g of $FeCl_3{\cdot}6H_2O$ was dissolved in 200 mL of deionized H_2O and titrated with 2 M NaOH until it reached pH ≈ 5. The solution was further titrated with 0.2 M NaOH until the target pH of 7.2–7.4. The suspension was equilibrated at this pH for 24 hours followed by a final pH adjustment with 0.2 M NaOH if a drift was observed. The Fh was then centrifuged at 5000 rpm for 15 min and washed 3× with deionized H_2O. After the third wash, the Fh suspension

was concentrated by removing most of the DI in the supernatant.

The Fh paste was transferred inside the glove box, and a volume of 10 mL degassed and deoxygenated DI-H_2O was added to the tube, which was vortexed to form a well-mixed homogenized suspension. This suspension was further degassed by sparging N_2-gas for 24 hours inside the glove box. Lastly, ferrihydrite suspension density was calculated by dissolving a volume of Fh in 4 M HCl. The Fe(III) in solution was determined by ICP-OES, Perkin-Elmer.

2.2 Thermogravimetric analysis – mass spectroscopy

A Netzsch Instruments TG-209F1 thermogravimetric analyzer was used to heat the samples from ~25 to 500 °C with a heating ramp of 2 K min^{-1} under 10 mL min^{-1} N_2 flow. Simultaneous examination of evolved dehydration/dihydroxylation products was performed with an in-line Aeolos QMS-403C mass spectrometer. Generally, 3–6 mg of sample were analyzed while monitoring ion currents (mass/charge, m/z) corresponding to H_2O (m/z = 18) and OH (m/z = 17).

For the samples subjected to different combinations of air and glovebox ageing regimes, samples were analyzed using a Netzsch Instruments TG 209 F1 Libra thermogravimetric analyzer coupled with a QMS 403 Aeolos Quadro mass spectrometer from ~25 to 500 °C with a heating ramp of 2 K min^{-1} under 10 mL min^{-1} N_2 flow. During these measurements, ion currents (mass/charge, m/z) corresponding to H_2O (m/z = 18), OH (m/z = 17), and CO_2(m/z = 44) were monitored.

To assist in the interpretation of thermogravimetric – mass spectrometry (TGA-MS) results for aged Fh samples that contain Gt [α-FeO(OH)] as an alteration product, we determined the dehydration behavior of a synthetic nanosized Gt. This sample, whose synthesis has been previously described,[58,59] has a N_2 Brunauer–Emmett–Teller (BET) specific surface area (SSA) of 115 ± 5 m^2 g^{-1}.

2.3 Scanning electron microscopy

SEM was performed using an FEI Helios NanoLab 600i field emission electron microscope. High resolution/high magnification secondary electron images were collected at an accelerating voltage of 3 kV and a beam current of 0.17 nA in immersion mode using a through-the-lens (TLD) detector. Images were collected at a working distance of 3.5–4 mm. The SEM analyses were performed after a few drops of Fh suspension were dropped onto Al-holders and dried in the N_2 chamber until analysis. The samples were coated with ~5–7 nm of carbon to minimize imaging artifacts due to charging.

2.4 X-ray diffraction

Powder X-ray diffraction (XRD) was performed on freeze-dried anaerobic powders packed into zero-background holders. Data were collected using a PANalytical X'Pert Bragg–Brentano diffractometer with Cu-K_α radiation (λ = 1.5418 Å), a graphite post-diffraction monochromator, and variable divergence and anti-scatter slits (illuminated length = 10 mm). Rietveld fitting (Topas v6, Bruker AXS) was used to quantify the amounts of Fh, Gt, and Hm The "Fhyd3" Fh structure published by Michel *et al.*[15] was used with only the scale factor refined. Cell parameters of a = 6.065 Å and c = 9.025 Å, and 1.4 nm Lorentz crystallite size broadening were used along with a linear background to avoid the background compensating for the diffuse Fh signal. Quantitation of Fh by XRD is problematic and so was checked by adding a weighted quantity of corundum (NIST SRM 676a) to selected samples. This allowed the absolute concentrations of Hm and Gt to be measured, and Fh concentration was calculated as the difference from 100%.

2.5 X-ray absorption spectroscopy and X-ray magnetic dichroism

X-ray absorption spectra were collected on beamline 6.3.1 at the Advanced Light Source (ALS), Lawrence Berkeley National Laboratory, California.[60] The Fh suspensions were deposited on indium foil, in a nitrogen-filled glovebox (for samples aged anaerobically) or in air (for samples aged aerobically), and allowed to dry. After drying, excess powder was removed and the remaining powder was pressed into the indium foil. The indium foil samples were then attached to the copper sample manipulator using silver paint and loaded into the end station under anaerobic conditions. The sample was positioned with the X-ray beam entering parallel to the magnetic field and perpendicular to the sample surface. The sample manipulator was cooled to 20 K using liquid helium for the Fe L-edge measurements, while the O K-edge measurements were made at room temperature. The XAS signal was monitored in total electron yield (TEY) mode, giving an effective probing depth of ~4.5 nm. Flying scans were collected at +1.8 tesla (T) then −1.8 T. The XAS spectra of the two magnetization directions were normalized to the incident beam intensity and subtracted from each other, to obtain the XMCD spectrum.[51]

2.6 Simulations of Fe L-edge XMCD

To perform a linear combination fit of the experimental Fe $L_{2,3}$-edges XMCD spectra of Fh as function of ageing, theoretical calculations of individual Fe $L_{2,3}$-edges XMCD components (*i.e.*, octahedral and tetrahedral Fe^{3+}) spectra have been performed using the ligand field multiplet approach developed by de Groot *et al.*[61] and following the methodology developed by Brice-Profeta *et al.*[62] The linear combination fit of the experimental O K-edge XANES spectra of Fh as function of ageing used the O K-edge spectra for O^{2-} and OH^- components calculated in previous work[56] using the FDMNES program.[63]

3. Results and discussion

3.1 Phase evolution

XRD measurements have been carried out to quantify the phase transformation of naturally aged 2-line Fh under

anaerobic conditions over a period of 1749 days. As shown in Fig. 1a, the initial (day 1) XRD pattern is characteristic of 2-line Fh with only two broad peaks present, reaching a maximum intensity at 2θ = 35° and 62°. The detection of several sharper diffraction peaks, characteristic of Hm and Gt crystals, were observed for samples older than 113 days. The presence of 6-line Fh was not detected. As shown in Fig. 1b, the time-dependent phase fraction analysis of the samples synthesized and aged under anaerobic conditions indicates that over a period of 1749 days about 70% of Fh has been transformed leading to the formation of Gt up to about 65% and a small fraction of Hm of about 5%, which remained similar for the whole timelapse. The time-evolution increase of the Gt phase fraction calculated from TGA-MS measurements shows a good agreement with the XRD analysis and is reported in Fig. 1b by filled square symbols. XRD analysis of naturally aged Fh samples synthesized and aged in aerobic conditions for 1596 days (open triangles in Fig. 1b) indicates a phase fraction for Fh, Gt, and Hm similar to the samples synthesized and aged in anaerobic conditions. This suggests that the synthesis and storage conditions do not affect the relative amount of the end-products, as well as the transformation rate. In the case of anaerobically synthesized and aged samples, further analysis, shown in Fig. 1c, suggests that the size of formed Gt particles steadily increases from about 13 nm to 25 nm within the first 600 days then tends to stabilize around 25 nm for samples older than 600 days.

During Fh ageing in anaerobic conditions, the samples had a pH of 4.5 ± 0.5 (see Fig. S1†) for which the transformation to Gt is generally preferred over that of Hm. While this result is in agreement with previous experiments conducted by Schwertmann *et al.*[31,37] who also monitored the natural transformation of Fh in aerated aqueous suspension, the XRD phase fraction analysis suggests that the rate of conversion of 2-line Fh under anaerobic conditions is slower than reported at similar pH values. At room temperature and pH = 4.5, Schwertmann *et al.* found that the conversion of 50% Fh into a mixture of Gt and Hm occurred in about 225 days. However, Fig. 1b shows that in 225 days only 21% of Fh has been converted into 15% Gt and 6% Hm. Under the anaerobic conditions of this study, Fh half-conversion was reached at 707 days, which is more than 3 times slower than at the conditions (*i.e.*, ambient temperature and aqueous suspension) of the experiments performed by Schwertmann *et al.* As the XRD determined phase fraction for the 1596 days old Fh synthesized and aged in aerobic conditions are similar to that of anaerobic conditions (Fig. 1b), we assume that slower transformation rate that we observe is due to other factors, such as the loading density of Fh particles and/or the method used to maintain constant pH in the experiments performed by Schwertmann *et al.*

To examine the extent of differences in Fh suspension pH we conducted experiments where we synthesized and aged Fh under four different permutations of synthesis and aging conditions (*i.e.*, synthesized in aerobic conditions and

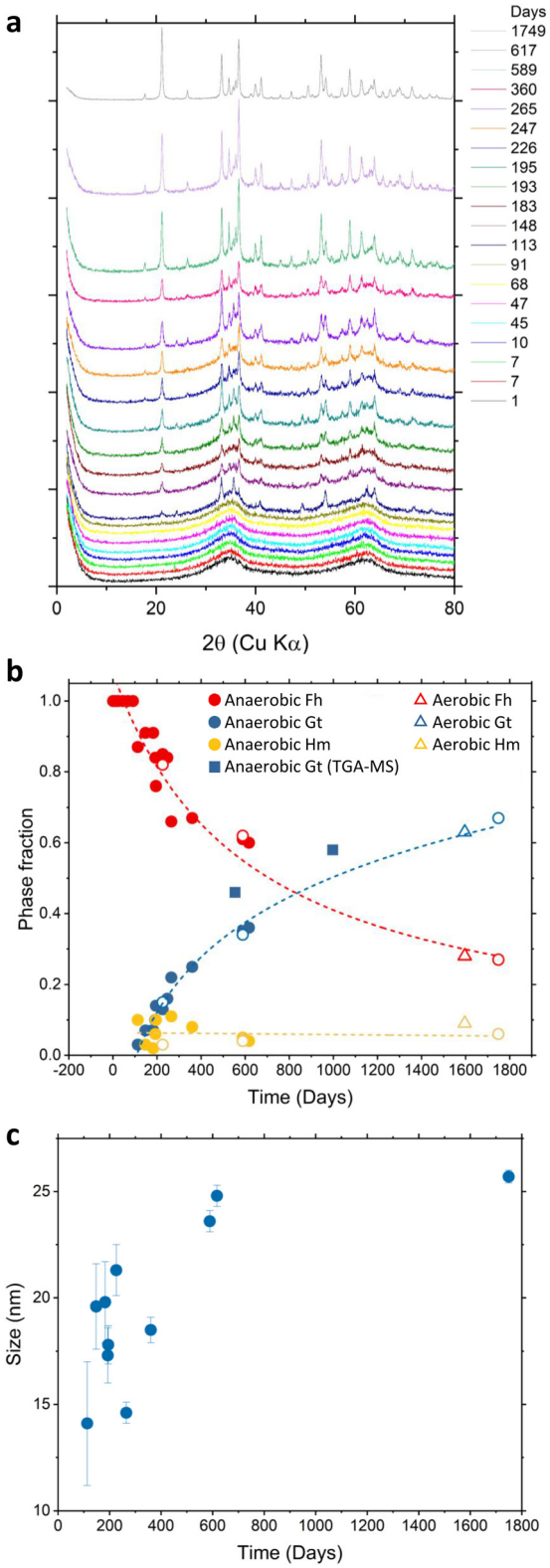

Fig. 1 (a) Evolution of the XRD pattern of naturally aged Fh under anaerobic conditions from 1 to 1749 days showing the appearance of Hm and Gt phases starting 113 days. (b) Time-evolution of the phase fraction present as function of Fh ageing under anaerobic conditions. Data are compared to companion anaerobic Gt fraction determined by TGA-MS (filled squares) and compared to a 1596 day old Fh sample aged under aerobic conditions (open triangles). (c) Particle size analysis of Gt as function of ageing under anaerobic conditions.

anaerobic conditions and aged in aerobic and anaerobic conditions for both synthesis methods). We observed only minor differences in pH, which varied over approximately 1 pH unit (pH 5.0 ± 0.5) between aging conditions and batches (see Fig. S2†). While there were some differences during the first month between the treatments, the pH stabilized to within 0.5 pH unit after 30 days. pH variability alone (see Table S1†) does not appear to be significant enough to explain differences in observed phase evolution to differences in pH.

In addition to changes in pH, we expect that the other variable which would be different between aerobically synthesized and aged and anaerobically synthesized and aged Fh would be the presence and amount of dissolved and sorbed CO_2. Even at relatively low pH, where dissolved CO_2 is in equilibrium with carbonic acid (H_2CO_3, pK_{a1} = 6.3), significant amounts of sorbed CO_2 are expected to be present at the Fh surface.[64–66] Consistent with these previous studies we measured 0.54 to 1.42 mM total inorganic carbon (TIC) (see ESI† material for methods) in Fh suspensions synthesized and aged in aerobic conditions (see Table S1†), compared to 0.0128 mM in deionized water in equilibrium with air. These values of TIC in Fh suspensions were within an order of magnitude of surface complexation model predictions[64,65,67] (see Fig. S3†) of approximately 5.5 mM TIC in Fh suspensions. We observe a significant difference in suspension TIC as a function of synthesis conditions of aerobic synthesis (mean = 0.95 mM) *vs.* anaerobic synthesis (mean = 0.42 mM) (Table S1,† p = 0.006). Despite our best efforts to remove CO_2, we still observed considerable TIC in anaerobically synthesized Fh, likely due to residual CO_2 in the sodium hydroxide used during Fh synthesis. However, we did not observe statistically significant differences in suspension TIC as a function of aging condition (*e.g.*, aerobically synthesized/anaerobically aged *vs.* aerobic/aerobic) over approximately two weeks (data shown in Table S1,† p = 0.35) regardless of starting synthesis condition. Finally, we conducted an experiment where we attempted removal of CO_2 from an aerobically synthesized and aged Fh suspension by bubbling it with 99.999% N_2 gas and measured pH and TIC content over time (see Fig. S4†). As expected with the loss of CO_2, the pH increased by 0.35 pH units and TIC decreased from 1.32 to 1.11 mM, suggesting that some bound CO_2 can be removed by a change in atmosphere, but that either considerable time for this equilibration is required or that CO_2 is very strongly bound to the surface of Fh and not easily removed.

To complement the XRD analysis, SEM images of the Fh samples synthesized in aerobic and naturally aged under anaerobic conditions were taken at 21, 283, 438, and 670 days, as shown in Fig. 2. Within the amorphous mass of Fh, one can readily observe the emergence of Gt and Hm crystallites for samples older than 113 days. In these images, Hm crystals have a distinguishable rhombohedral shape while Gt crystals have a nanorod shape. Additional SEM images showing the time-evolution of Fh samples synthesized in aerobic and aged in anaerobic conditions from 21 days to 670 days are shown in Fig. S5.†

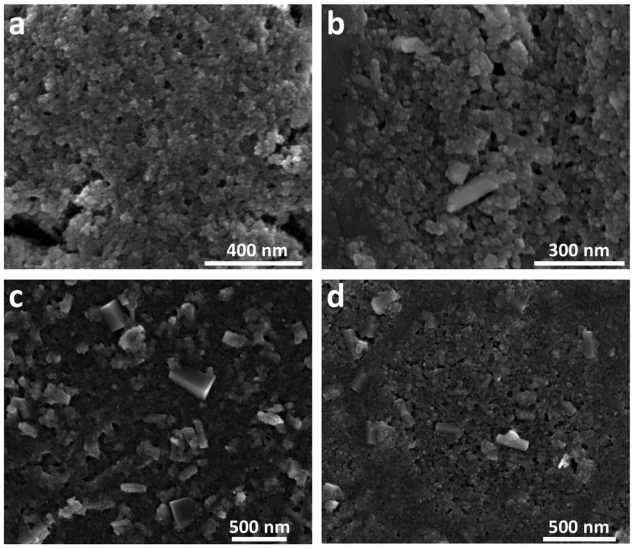

Fig. 2 SEM images showing the time-evolution of naturally aged Fh samples under anaerobic conditions taken approximately at (a) 21 days, (b) 283 days, (c) 438 days, and (d) 670 days. Additional SEM images are shown in Fig. S5.†

3.2 Evolution of hydration during Fh ageing and impact of synthesis and storage conditions for fresh Fh

The TGA-MS analysis of three Fh samples, synthesized in aerobic and aged under anaerobic conditions for 7 days, 554 days, and 994 days revealed 17–19% mass loss from 25–500 °C, as shown in Fig. 3. The Fh sample aged for 7 days displayed a smooth and continuous weight loss, as shown in Fig. 3a, as it transformed to Hm. A prominent weight loss region corresponding to the coincident H_2O and OH ion current peaks at 60 °C from physisorbed water, along with distinct shoulders at ~110 °C, was observed. The release of residual water during thermal decomposition of Fh is apparent from the slight elevation in m/z 18 ion current at ~380 °C (inset in Fig. 3a), corresponding to the thermal transformation of Fh to Hm.[68] The thermal decomposition of Fh in this study is broadly consistent with previously reported descriptions.[8,69–72]

In the case of 554 and 994 days old Fh samples, the ageing resulted in changes to TGA-MS signatures, as evolved H_2O and OH was observed at ~260 °C, along with a corresponding weight loss step, as shown in Fig. 3b and c. These new features are consistent with the release of chemically bound water of alteration product Gt in the aged Fh samples during thermal decomposition,[73–75,77] and they are in general agreement with the TGA-MS behavior of our nano-Gt sample (see Fig. S6†). A notable difference between the TGA-MS results of the 7 days aged and long-term (≥554 days) aged samples is the absence of the H_2O/OH shoulder at ~110 °C in the latter. We therefore suggest that the absence of this feature in aged sample is due to

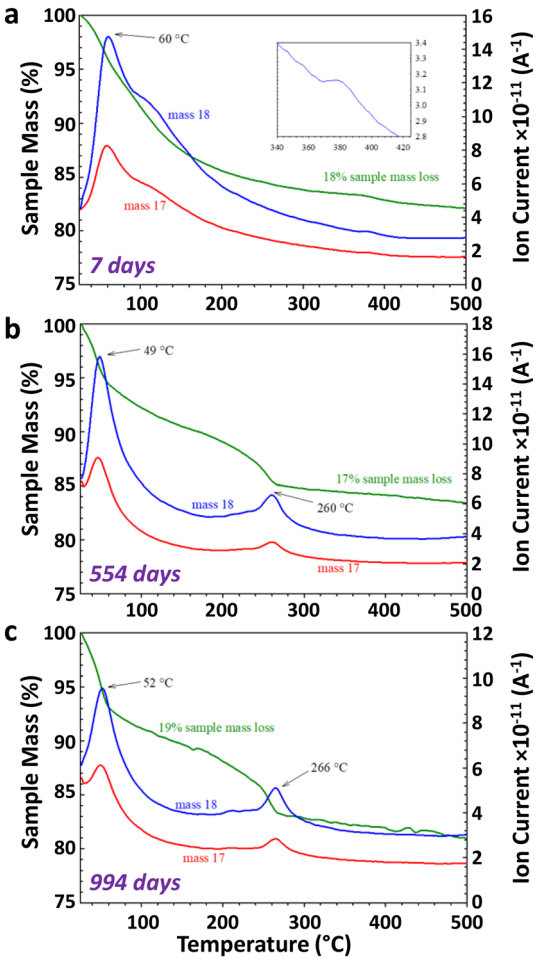

Fig. 3 TGA-MS analysis for three naturally aged Fh samples synthesized in aerobic and aged in anaerobic conditions of (a) 7 days, (b) 554 days, and (c) 994 days that shows mass loss (left *y*-axis) and ion current curves (right *y*-axis) as a function of temperature.

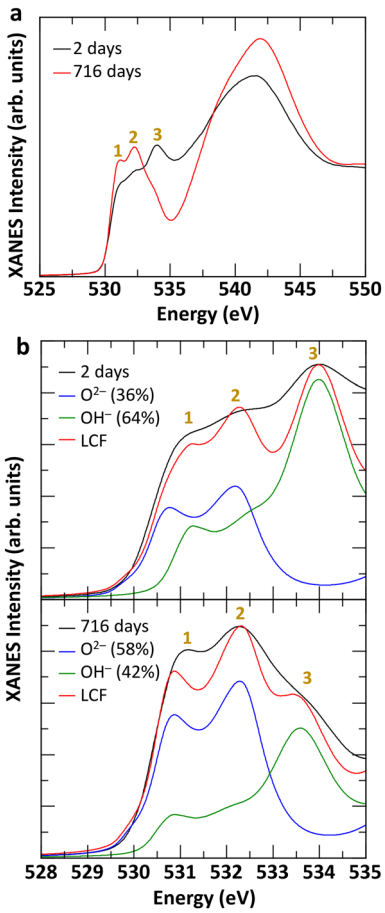

Fig. 4 (a) Comparison of the O K-edge XANES spectra for fresh (2 days) and 716 days old Fh samples synthesized in aerobic and aged in anaerobic conditions. (b) The linear combination fits (LCF) of the experimental spectra with calculated O^{2-} and OH^- contributions indicates that the peaks labelled 1 and 2 are associated with O^{2-} species, while the peak labelled 3 is associated with OH^- species.

the facile removal of the OH in the 7 days old Fh sample. This interpretation is consistent with the O K-edge XANES spectral changes shown in Fig. 4 between fresh and old Fh samples highlighting the evolution of structural hydration of Fh as function of ageing. As shown in Fig. 4a, the spectra for fresh (2 days) and 716 days old Fh samples present different spectral features. Based on previous theoretical analysis of O K-edge spectra in Gt,[56] the higher energy peak, labelled 3 at 533–535 eV, is representative of hydroxyl groups (OH^-), while the lower energy peaks, labelled 1 and 2, located in between 530–533 eV are associated with O^{2-} species. The fresh Fh sample has a prominent hydroxyl peak at ~534 eV, whereas a similar peak is not distinguishable for the 716 days old Fh sample. As shown in Fig. 4b, a linear combination fit of the O K-edge spectra of fresh and 716 days old samples using theoretically calculated O^{2-} and OH^- components suggests a dehydration of 22%. While the fresh Fh sample has a larger contribution from OH^- component compared to O^{2-}, the 716 days old Fh sample has a larger contribution from O^{2-}, with a O^{2-}/OH^- ratio closer to 1. The time-evolution of the O K-edge XANES spectra from progressively more-aged samples (from 2 to 716 days shown in Fig. S7†) exhibit concomitant decreasing OH-associated peak 3 with increasing lower energy O^{2-} species-associated peak 1 and 2.

This labile OH population likely consists of singly coordinated isolated hydroxyls (–OH) at the Fh surface, recently spectroscopically delineated by Boily and Song.[72] They performed chemometric interpretations of temperature controlled *in situ* infrared spectroscopy coupled with mass spectrometry (IR-MS) to distinguish between the –OH (removed at ~134 °C *in vacuo*) and doubly-coordinated hydroxyl groups (μ-OH), showing that μ-OH is removed at higher temperatures (~204 °C). As triply-coordinated μ_3-OH sites weren't detected by Boily and Song,[72] it is likely that μ-OH groups were the sole surface species of the aged Fh. It is important to understand the relatively rapid removal of isolated hydroxyls during anaerobic ageing as the evolving surface chemistry dictates the catalytic reactivity of Fh. As highlighted by Boily and Song,[72] the long-term behavior of Fh coordination environments has implications for Fh reactivity towards environmentally-relevant gasses and

organics, along with Fh–Fh interactions that control nanoparticle aggregation.

TGA-MS measurements conducted on (~7–14 days old) Fh samples that were synthesized and aged in four combinations of aerobic and anaerobic environments showed limited variability in thermal decomposition curves and mass spectrometry signals, including for m/z = 44, a measure of CO_2 incorporation during synthesis and transformation during ageing (see Fig. S8†). Based on the weight losses that coincide with detection of OH and H_2O (m/z = 17 and 18), the samples contained ~3–7 wt% Gt.

3.3 Evolution of Fe site type populations during Fh ageing

The evolution of tetrahedral *versus* octahedral iron sites in Fh as function of ageing time was monitored by measuring the Fe $L_{2,3}$-edges XANES and XMCD spectra and quantifying the changes in spectral peak intensities. As Gt and Hm are predominantly antiferromagnetic and saturate magnetically at 57 T and 3 T respectively,[76] the XMCD signal measured at a field strength of 1.8 T is dominantly from Fh. The time-evolution of Fe $L_{2,3}$-edges XANES and XMCD spectra for Fh samples of 7, 30, 112, and 207 days old synthesized in aerobic and aged in anaerobic conditions are shown in Fig. 5. We note that the XANES and XMCD spectra measured present features similar to those obtained by Guyodo *et al.*[52] who examined 6-line Fh. In particular, the presence of an intense positive peak in the XMCD signal at about 709 eV, which based on previous theoretical simulations of Fe $L_{2,3}$-edges XANES and XMCD of magnetite,[77] clearly indicates the presence of tetrahedral Fe(III) in the samples. The fact that an XMCD spectra signal is observable at all indicates the presence of a magnetic moment in the Fh, arising from the imperfect cancelation of tetrahedral and octahedral site spin sublattices coupled antiparallel.[21,78] In addition to this magnetically ordered Fe fraction observable by XMCD, the presence of tetrahedral Fe in the L-edge XANES spectra (magnetically ordered and disordered contributions) can also be observed by the filling of the minimum between the pre- and main-edges in Fig. 5a (labelled Fe^T). In Fig. 5b, the XMCD signal for tetrahedral Fe(III) can be seen to gradually decrease as Fh ages, thereby indicating that the 7 days old 2-line Fh, stored under anaerobic conditions, contains more tetrahedral Fe(III) than older samples. This is also seen in the Fe L-edge XANES in Fig. 5a for which the intensity of the minimum between pre- and main-edges decreases.

In order to quantify the evolution of the octahedral (Fe^O(III)) and tetrahedral (Fe^T(III)) iron site population in Fh as function of ageing, we performed a linear combination fit (LCF) of the XMCD spectra with two individual Fe(III) components, as shown in Fig. S9.† The contribution of the tetrahedral Fe(III) component as function of ageing time is shown in Fig. 6. For fresh Fh samples the amount of tetrahedral Fe is similar to that of octahedral Fe with a contribution of 50% to the XMCD signal. This indicates that for fresh 2-line Fh that there are as many tetrahedral Fe as octahedral Fe sites, substantially more than nominally expected based on the amount of tetrahedral Fh in the defect-free Fh model of Michel *et al.*,[15] which ideally contains 20% of tetrahedral sites, and larger than the value of 28 ± 3% reported by Guyodo *et al.*[52] for 6-line Fh. Because the latter study showed that XMCD collected at the Fe L-edge in more surface-sensitive total electron yield mode (as was done in the present study) gives similar results to more penetrating Fe K-edge XMCD collected in total fluorescence yield mode, the large proportion of Fe^T(III) we observe is unlikely to reflect enrichment of these sites at Fh surfaces. Rather, the high initial proportion of Fe^T(III) appears to be intrinsic to fresh 2-line Fh aged anaerobically. However, Fig. 6 shows that the tetrahedral contribution to the XMCD signal gradually decreases as Fh ages. After 100 days, the contribution of

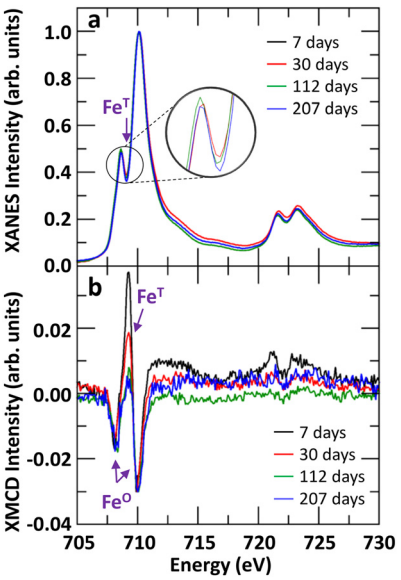

Fig. 5 Time-evolution of the Fe L-edge (a) XANES and corresponding (b) XMCD spectra for Fh samples synthesized in aerobic and aged in anaerobic conditions for a duration of 7, 30, 112, and 207 days. The peaks associated to tetrahedral and octahedral Fe(III) are labelled as Fe^T and Fe^O respectively.

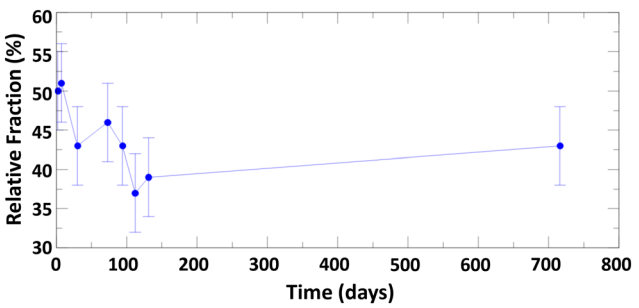

Fig. 6 Time-evolution of the relative fraction of Fe(III) tetrahedral sites in Fh samples synthesized in aerobic conditions and aged in anaerobic conditions as function of ageing. The estimated error on the relative fractions has been represented by vertical lines at each point.

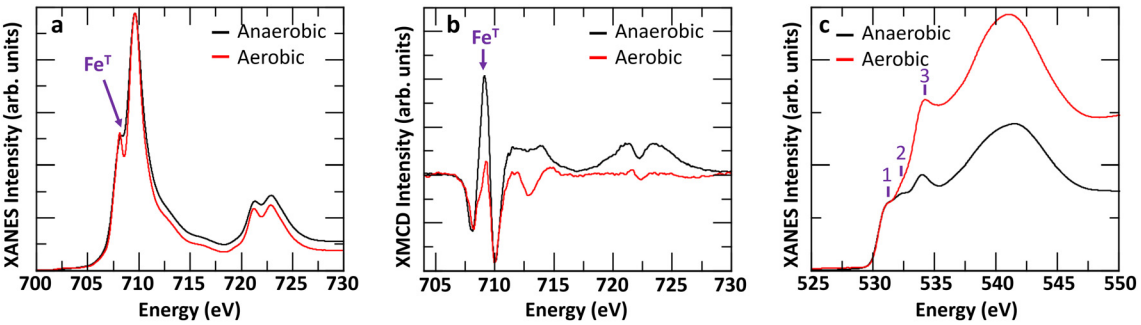

Fig. 7 (a) Comparison of Fe $L_{2,3}$-edges XANES, (b) XMCD, and (c) O K-edge XANES of fresh Fh samples (2 days old) synthesized in aerobic conditions and aged in either aerobic or anaerobic conditions.

tetrahedral Fe sites has decreased to a lower limit of about 40 ± 5%, closer to the estimation for 6-line Fh.[52]

The difference may also arise, at least in part, due to anaerobic conditions stabilizing more tetrahedral Fe sites in Fh compared to more commonly used aerobic conditions.[15,52] To evaluate this prospect, we synthesized 2-line Fh samples in aerobic conditions and aged the fresh samples in either aerobic or anaerobic conditions for 2 days. A comparison of the Fe $L_{2,3}$-edges XANES and XMCD, and O K-edge XANES spectra is shown in Fig. 7. The results clearly indicate that anaerobic ageing conditions favor the formation of tetrahedral iron compared to aerobic ageing conditions. As shown in Fig. 7a, the minimum between the pre- and main-edge in Fe $L_{2,3}$-edges XANES spectra is more filled for Fh aged in anaerobic than in aerobic conditions. This is consistent with a more intense XMCD peak at ~709 eV in Fig. 7b, associated with tetrahedral Fe(III). A linear combination fit of the aerobic and anaerobic XMCD signals respectively yields 37% and 50% tetrahedral Fe(III), as shown in Fig. S10a and b.† Given that the observed amount of 37% tetrahedral Fe for fresh Fh samples aged in aerobic conditions is associated with a Fh sample only 2 days old, and that from the anaerobic ageing behavior (Fig. 6) we observed a steady decrease with further aging, we can expect a similar decrease in the aerobic aging case. This would likely bring the amount of tetrahedral Fe in aerobic aged 2-line Fh samples close to the value determined for 6-line Fh by Guyodo *et al.*[52]

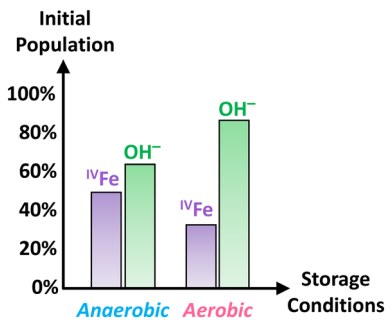

Fig. 8 Summary of the initial tetrahedral Fe and OH^- population trends obtained for fresh Fh samples aged in either anaerobic or aerobic conditions.

In addition, the O K-edge XANES spectra, shown in Fig. 7c, for both experimental conditions suggests that Fh samples maintained in aerobic conditions are more hydrated than those maintained in anaerobic conditions as peak #3, associated with the OH^- contribution, is more intense relative to the O^{2-} contribution. A linear combination fit of the two O K-edge XANES spectra, shown in Fig. S10c and d,† yields OH^- contributions of 87% and 64% for Fh aged in aerobic and anaerobic conditions, respectively. This further implies a potential interdependence between the amount of hydroxyl content and that of tetrahedral Fe(III) in the samples, such that the relative proportion of tetrahedral Fe(III) in Fh is smaller as the hydroxyl contribution gets larger. As one possible mechanistic explanation, the apparently larger hydroxyl content and lower tetrahedral Fe(III) proportion detected in the aerobically aged Fh may reflect conversion of some fraction of the latter to octahedral Fe(III) by saturation of some of the available coordination sites on tetrahedral Fe(III) with OH^-. Analysis of Fe L-edge XMCD for additionally tested fresh Fh in the mixed combination of aerobic/anaerobic synthesis and ageing conditions is shown in Fig. S11,† which confirms the trend that fresh Fh aged in anaerobic conditions has more than 40% tetrahedral Fe, while the samples aged in aerobic conditions have less than 40% tetrahedral Fe, regardless of their synthesis condition. Fig. 8 summarizes the initial OH^- and tetrahedral Fe (^{IV}Fe) trends for fresh Fh samples stored in either aerobic or anaerobic conditions.

4. Conclusions

Key structural and compositional properties of 2-line Fh have been measured as a function of ageing time, and aerobic *versus* anaerobic conditions during synthesis and storage. The overall findings suggest that for fresh Fh samples, the tetrahedral iron and hydroxyl populations are correlated and that their initial population is more dependent on storage conditions rather than those at synthesis. For fresh Fh stored in anaerobic conditions, the initial tetrahedral iron population is larger and the hydroxyl population is lower than Fh stored in aerobic conditions. With ageing, those two populations decrease over time, consistent with an

interdependence between them. Despite these structural and compositional differences at early ageing timescales, aerobic *versus* anaerobic storage conditions do not affect the long-term transformation rate to more stable Gt and Hm, nor the relative proportion of these product phases produced. This is consistent with similar pH and TIC characteristics across the sample set. Nonetheless, our findings highlight the impact of storage conditions on the structure and hydration of Fh at early stages, clearly indicating the importance of differentiating Fh samples on the basis of both age and environmental conditions during ageing.

Conflicts of interest

There are no conflicts of interest to declare.

Acknowledgements

This material is based upon work supported by the U.S. Department of Energy, Office of Science, Office of Basic Energy Sciences, Chemical Sciences, Geosciences, and Biosciences Division through its Geosciences program at Pacific Northwest National Laboratory (FWP 56674). PNNL is a multi-program national laboratory operated for the DOE by Battelle Memorial Institute under Contract No. DE-AC05-76RL01830. Computational resources were provided by PNNL Institutional Computing (PIC). This research used resources of the Advanced Light Source, which is a DOE Office of Science User Facility under contract no. DE-AC02-05CH11231.

References

1 F. V. Chukhrov, B. B. Zvyagin, A. I. Gorshkov, L. P. Yermilova and V. V. Balashova, Ferrihydrite, *Izvestiya. Akad. Nauk. SSSR, Ser. Geol.*, 1973, **4**, 23–33 (*Int. Geol. Rev.*, 1996, **16**, 1131–1143).

2 R. M. Cornell and U. Schwertmann, *The iron oxides: structure, properties, reactions, occurrences and uses*, Wiley-VCH: Weinheim, Cambridge, 2nd edn, 2003.

3 S. Jenssen, F. Larsen, C. B. Koch and E. Arvin, Sorption and desorption of arsenic to ferrihydrite in a sand filter, *Environ. Sci. Technol.*, 2005, **39**, 8045–8051.

4 N. A. Hodge, C. J. Kiely, R. Whyman, M. R. H. Siddiqui, G. J. Hutchings, Q. A. Pankhurst, F. E. Wagner, R. R. Rajaram and S. E. Golinski, Microsctructural comparison of calcined and uncalcined gold/iron-oxide catalysts for low-temperature CO oxidation, *Catal. Today*, 2002, **72**, 133–144.

5 M. F. Hochella, S. K. Lower, P. A. Maurice, R. L. Penn, N. Sahai, D. L. Sparks and B. S. Twining, Nanominerals, mineral nanoparticles, and Earth systems, *Science*, 2008, **319**, 1631–1635.

6 C. W. Childs, Ferrihydrite: A review of structure, properties and occurrence in relation to soils, *Z. Pflanzenernahr. Bodenk*, 1992, **155**, 441–448.

7 L. Carlson and U. Schwertmann, Natural ferrihydrites in surface deposits from Finland and their association with silica, *Geochim. Cosmochim. Acta*, 1981, **45**, 421–429.

8 F. M. Michel, L. Ehm, G. Liu, W. Q. Han, S. M. Antao, P. J. Chupas, P. L. Lee, K. Knorr, H. Eulert, J. Kim, C. P. Grey, A. J. Celestian, J. Gillow, M. A. A. Schoonen, D. R. Strongin and J. B. Parise, Similarities in 2- and 6-line ferrihydrite based on pair distribution function analysis of X-ray total scattering, *Chem. Mater.*, 2007, **19**, 1489–1496.

9 X. Wang, M. Zhu, L. K. Koopal, W. Li, W. Xu, F. Liu, J. Zhang, Q. Liu, X. Feng and D. L. Sparks, Effects Of Crystallite Size On The Structure And Magnetism Of Ferrihydrite, *Environ. Sci.: Nano*, 2016, **3**, 190–202.

10 H. F. Chappell, W. Thom, D. T. Bowron, N. Faria, P. J. Hasnip and J. J. Powell, Structure of naturally hydrated ferrihydrite revealed through neutron diffraction and first-principles modeling, *Phys. Rev. Mater.*, 2017, **1**, 036002.

11 H. Liu, X. Li, Y. Wang, X. Yang, Z. Zhen, R. Chen, D. Hu and Y. Wei, New insight into the effect of the formation environment of ferrihydrite on its structure and properties, *RSC Adv.*, 2014, **4**, 11451.

12 F. M. Michel, V. Barron, J. Torrent, M. P. Morales, C. J. Serna, J. F. Boily, Q. S. Liu, A. Ambrosini, A. C. Cismasu and G. E. Brown, Ordered ferrimagnetic form of ferrihydrite reveals links among structure, composition, and magnetism, *Proc. Natl. Acad. Sci. U. S. A.*, 2010, **107**, 2787–2792.

13 A. Navrotsky, L. Mazeina and J. Majzlan, Size-driven structural and thermodynamic complexity in iron oxides, *Science*, 2008, **319**, 1635–1638.

14 J. L. Jambor and J. E. Dutrizac, Occurrence and constitution of natural and synthetic ferrihydrite, a widespread iron oxyhydroxide, *Chem. Rev.*, 1998, **98**, 2549–2585.

15 F. M. Michel, L. Ehm, S. M. Antao, P. L. Lee, P. J. Chupas, G. Liu, D. R. Strongin, M. A. A. Schoonen, B. L. Phillips and J. B. Parise, The structure of ferrihydrite, a nanocrystalline material, *Science*, 2007, **316**, 1726–1729.

16 A. Manceau, S. Skanthakumar and L. Soderholm, PDF analysis of ferrihydrite: Critical assessment of the under-constrained akdalaite model, *Am. Mineral.*, 2014, **99**, 102–108.

17 N. P. Funnell, M. F. Fulford, S. Inoué, K. Kletetschka, F. M. Michel and A. L. Goodwin, Nanocomposite structure of two-line ferrihydrite powder from total scattering, *Commun. Chem.*, 2020, **22**, 1.

18 V. A. Drits, B. A. Sakharov, A. L. Salyn and A. Manceau, Structural model for ferrihydrite, *Clays Clay Miner.*, 1993, **28**, 185–208.

19 B. Gilbert, J. J. Erbs, R. L. Penn, V. Petkov, D. Spagnoli and G. A. A. Waychunas, Disordered nanoparticle model for 6-line ferrihydrite, *Am. Mineral.*, 2013, **98**, 1465–1476.

20 U. Schwertmann and R. M. Cornell, *Iron oxides in the laboratory: preparation and characterization*, VCH: Weinheim Cambridge, 1991.

21 M. Sassi and K. M. Rosso, Roles of Hydration and Magnetism on the Structure of Ferrihydrite from First Principles, *ACS Earth Space Chem.*, 2019, **3**, 70–78.

22 M. Sassi, A. M. Chaka and K. M. Rosso, Ab initio thermodynamics reveals the nanocomposite structure of ferrihydrite, *Commun. Chem.*, 2021, **4**, 134.

23 J. M. Byrne and A. Kappler, A revised analysis of ferrihydrite at liquid helium temperature using Mössbauer spectroscopy, *Am. Mineral.*, 2022, **107**, 1643–1651.

24 C. M. Cardile, Tetrahedral Fe^{3+} in Ferrihydrite: ^{57}Fe Möossbauer Spectroscopic Evidence, *Clays Clay Miner.*, 1988, **36**, 537–539.
25 Q. A. Pankhurst and R. J. Pollard, Structural and Magnetic Properties of Ferrihydrite, *Clays Clay Miner.*, 1992, **40**, 268–272.
26 F. Maillot, G. Morin, Y. H. Wang, D. Bonnin, P. Ildefonse, C. Chaneac and G. Calas, New insight into the structure of nanocrystalline ferrihydrite: EXAFS evidence for tetrahedrally coordinated iron(III), *Geochim. Cosmochim. Acta*, 2011, **75**, 2708–2720.
27 Y. Guyodo, P. Sainctavit, M. A. Arrio, C. Carvallo, R. L. Penn, J. J. Erbs, B. S. Forsberg, G. Morin, F. Maillot, F. Lagroix, P. Bonville, F. Wilhelm and A. Rogalev, X-ray magnetic circular dichroism provides strong evidence for tetrahedral iron in ferrihydrite, *Geochem., Geophys., Geosyst.*, 2012, **13**, 9.
28 D. Peak and T. Regier, Direct Observation of Tetrahedrally Coordinated Fe(III) in Ferrihydrite, *Environ. Sci. Technol.*, 2012, **46**, 3163–3168.
29 J. Zhao, F. E. Huggins, Z. Feng, F. L. Lu, N. Shah and G. P. Huffman, Structures of a nanophase iron oxide catalyst, *J. Catal.*, 1993, **143**, 499–509.
30 J. M. Zhao, F. E. Huggins, Z. Feng and G. P. Huffman, Ferrihydrite; surface structure and its effects on phase transformation, *Clays Clay Miner.*, 1994, **42**, 737–746.
31 U. Schwertmann and E. Murad, Effect of pH on the formation of goethite and hematite from ferrihydrite, *Clays Clay Miner.*, 1983, **31**, 277–284.
32 R. K. Kukkadapu, J. M. Zachara, J. K. Frederickson, S. C. Smith, A. C. Dohnalkova and C. K. Russell, Transformation of 2-lines ferrihydrite to 6-line ferrihydrite under oxic and anoxic conditions, *Am. Mineral.*, 2003, **88**, 1903–1914.
33 H. Liu, M. R. Ma, M. Qin, L. J. Yang and Y. Wei, Studies on the controllable transformation of ferrihydrite, *J. Solid State Chem.*, 2010, **183**, 2045–2050.
34 V. M. Yuwono, N. D. Burrows, J. A. Soltis and R. L. Penn, Oriented aggregation: Formation and transformation of mesocrystal intermediates revealed, *J. Am. Chem. Soc.*, 2010, **132**, 2163–2165.
35 O. Qafoku, L. Kovarik, M. E. Bowden, E. Nakouzi, A. Sheng, J. Liu, C. I. Pearce and K. M. Rosso, Nanoscale observations of Fe(II)-induced ferrihydrite transformation, *Environ. Sci.: Nano*, 2020, **7**, 2953–2967.
36 M. Sassi and K. M. Rosso, Ab Initio Evaluation of Solid-State Transformation Pathways from Ferrihydrite to Goethite, *ACS Earth Space Chem.*, 2022, **6**, 800–809.
37 U. Schwertmann, H. Syanjek and H.-H. Becher, Long-term in vitro transformation of 2-line ferrihydrite to goethite/hematite at 4, 10, 15 and 25°C, *Clay Miner.*, 2004, **39**, 433–438.
38 C. M. Hansel, S. G. Benner and S. Fendorf, Competing Fe(II)-Induced Mineralization Pathways of Ferrihydrite, *Environ. Sci. Technol.*, 2005, **39**, 7147–7153.
39 H. Liu, Y. Wei and Y. Sun, The formation of hematite from ferrihydrite using Fe(II) as a catalyst, *J. Mol. Catal. A: Chem.*, 2005, **226**, 135–140.
40 A. Sheng, J. Liu, X. Li, O. Qafoku, R. N. Collins, N. A. Jones, C. I. Pearce, C. Wang, J. Ni, A. Lu and K. M. Rosso, Labile Fe(III) from sorbed Fe(II) oxidation is the key intermediate in Fe(II)-catalyzed ferrihydrite transformation, *Geochim. Cosmochim. Acta*, 2020, **272**, 105–120.
41 A. Sheng, J. Liu, X. Li, L. Luo, Y. Ding, C. Chen, X. Zhang, C. Wang and K. M. Rosso, Labile Fe(III) supersaturation controls nucleation and properties of product phases from Fe(II)-catalyzed ferrihydrite transformation, *Geochim. Cosmochim. Acta*, 2021, **309**, 272–285.
42 A. Sheng, X. Li, Y. Arai, Y. Ding, K. M. Rosso and J. Liu, Citrate controls Fe(II)-catalyzed transformation of ferrihydrite by complexation of the labile Fe(III) intermediate, *Environ. Sci. Technol.*, 2020, **54**, 7309–7319.
43 D. Latta, K. M. Rosso and M. M. Scherer, Tracking Initial Fe(II)-Driven Ferrihydrite Transformations: A Mössbauer Spectroscopy and Isotope Investigation, *ACS Earth Space Chem.*, 2023, **7**, 1814–1824.
44 R. M. Cornell, R. Giovanoli and W. Schneider, Review of the hydrolysis of iron(III) and the crystallization of amorphous iron(III) hydroxide hydrate, *J. Chem. Technol. Biotechnol.*, 1989, **46**, 115–134.
45 P. R. Anderson and M. M. Benjamim, Effects of silicon on the crystallization and adsorption properties of ferric oxides, *Environ. Sci. Technol.*, 1985, **19**, 1048–1053.
46 A. S. Campbell, U. Schwertmann, H. Stanjek, J. Friedl, A. Kyek and P. A. Campbell, Si incorporation into hematite by heating Si-ferrihydrite, *Langmuir*, 2002, **18**, 7804–7809.
47 R. M. Cornell, R. Giovanoli and P. W. Schindler, Effect of silicate species on the transformation of ferrihydrite into geothite and hematite in alkaline media, *Clays Clay Miner.*, 1987, **35**, 21–28.
48 S. Das, M. J. Hendry and J. Essilfie-Dughan, Effects of adsorbed arsenate on the rate of transformation of 2-line ferrihydrite at pH 10, *Environ. Sci. Technol.*, 2011, **45**, 5557–5563.
49 N. Galvez, V. Barron and J. Torrent, Effect of phosphate on the crystallization of hematite, goethite, and lepidocrocite from ferrihydrite, *Clays Clay Miner.*, 1999, **47**, 304–311.
50 G. van der Laan and A. I. Figueroa, X-ray magnetic circular dichroism – A versatile tool to study magnetism, *Coord. Chem. Rev.*, 2014, **277–278**, 95–129.
51 R. A. D. Pattrick, G. Van Der Laan, C. Henderson, B. Michael, P. Kuiper, E. Dudzik and D. J. Vaughan, Cation site occupancy in spinel ferrites studied by X-ray magnetic circular dichroism: developing a method for mineralogists, *Eur. J. Mineral.*, 2002, **14**, 1095–1102.
52 Y. Guyodo, P. Sainctavit, M. A. Arrio, C. Carvallo, R. L. Penn, J. J. Erbs, B. S. Forsberg, G. Morin, F. Maillot, F. Lagroix, P. Bonville, F. Wilhelm and A. Rogalev, X-ray magnetic circular dichroism provides strong evidence for tetrahedral iron in ferrihydrite, *Geochem., Geophys., Geosyst.*, 2012, **13**, 1.
53 L. Cao, Z.-X. Jiang, Y.-H. Du, X.-M. Yin, S.-B. Xi, W. Wen, A. P. Roberts, A. T. S. Wee, Y.-M. Xiong, Q.-S. Liu and X.-Y. Gao, Origin of Magnetism in Hydrothermally Aged 2-Line Ferrihydrite Suspensions, *Environ. Sci. Technol.*, 2017, **51**, 2643–2651.

54 D. Bilardello, S. K. Banerjee, M. W. R. Volk, J. A. Soltis and R. Lee Penn, Simulation of Natural Iron Oxide Alteration in Soil:Conversion of Synthetic Ferrihydrite to Hematite Without Artificial Dopants Observed With Magnetic Methods, *Geochem., Geophys., Geosyst.*, 2020, **20**, 1–19.

55 A. R. B. de Castro, R. D. Zysler, M. Vasquez Mansilla, C. Arciprete and M. Dimitrijewits, Magnetic circular dichroism in nanostructured hematite, *J. Magn. Magn. Mater.*, 2001, **231**, 287–290.

56 L. Notini, D. E. Latta, A. Neumann, C. I. Pearce, M. Sassi, A. T. N'Diaye, K. M. Rosso and M. M. Scherer, The Role of Defects in Fe(II)–Goethite Electron Transfer, *Environ. Sci. Technol.*, 2018, **52**, 2751–2759.

57 R. L. Frost, Z. Ding and H. D. Ruan, Thermal analysis of goethite, *J. Therm. Anal. Calorim.*, 2003, **71**, 783–797.

58 R. M. Handler, A. J. Frierdich, C. M. Johnson, K. M. Rosso, B. L. Beard, C. Wang, D. E. Latta, A. Neumann, T. Pasakarnis, W. A. P. J. Premaratne and M. M. Scherer, Fe(II)-Catalyzed Recrystallization of Goethite Revisited, *Environ. Sci. Technol.*, 2014, **48**, 11302–11311.

59 R. M. Handler, B. L. Beard, C. M. Johnson and M. M. Scherer, Atom Exchange between Aqueous Fe(II) and Goethite: An Fe Isotope Tracer Study, *Environ. Sci. Technol.*, 2009, **43**, 1102–1107.

60 P. Nachimuthu, J. H. Underwood, C. D. Kemp, E. M. Gullikson, D. W. Lindle, D. K. Shuh and R. C. C. Perera, Performance Characteristics of Beamline 6.3.1 from 200 eV to 2000 eV at the Advanced Light Source, *AIP Conf. Proc.*, 2004, **705**, 454–457.

61 F. M. F. de Groot, J. C. Fuggle, B. T. Thole and G. A. Sawatzky, 2p X-ray absorption of 3d transition-metal compounds: An atomic multiplet description including the crystal field, *Phys. Rev. B: Condens. Matter Mater. Phys.*, 1990, **42**, 5459.

62 S. Brice-Profeta, M. A. Arrio, E. Tronc, N. Menguy, I. Letard, C. Cartier dit Moulin, M. Noguès, C. Chanéac, J. P. Jolivet and Ph. Sainctavit, Magnetic order in γ-Fe_2O_3 nanoparticles: a XMCD study, *J. Magn. Magn. Mater.*, 2005, **288**, 354–365.

63 Y. Joly, X-ray absorption near-edge structure calculations beyond the muffin-tin approximation, *Phys. Rev. B: Condens. Matter Mater. Phys.*, 2001, **63**, 125120.

64 C. A. J. Appelo, M. J. J. Van der Weiden, C. Tournassat and L. Charlet, Surface complexation of ferrous iron and carbonate on ferrihydrite and the mobilization of arsenic, *Environ. Sci. Technol.*, 2002, **36**, 3096–3103.

65 J. M. Zachara, D. C. Girvin, R. L. Schmidt and C. T. Resch, Chromate adsorption on amorphous iron oxyhydroxide in the presence of major groundwater ions, *Environ. Sci. Technol.*, 1987, **21**, 589–594.

66 J. C. Mendez and T. Hiemstra, Carbonate Adsorption to Ferrihydrite: Competitive Interaction with Phosphate for Use in Soil Systems, *ACS Earth Space Chem.*, 2019, **3**, 129–141.

67 D. A. Dzombak and F. M. M. Morel, *Surface Complexation Modeling: Hydrous Ferric Oxide*, John Wiley & Sons, New York, 1990, p. 393.

68 W. Xu, D. B. Hausner, R. Harrington, P. L. Lee, D. R. Strongin and J. B. Parise, Structural water in ferrihydrite and constraints this provides on possible structure models, *Am. Mineral.*, 2011, **96**, 513–520.

69 R. A. Eggleton and R. W. Fitzpatrick, New data and a revised structural model for ferrihydrite, *Clays Clay Miner.*, 1988, **36**, 111–124.

70 G. Rzepa, G. Pieczara, A. Gaweł, A. Tomczyk and R. Zalecki, The influence of silicate on transformation pathways of synthetic 2-line ferrihydrite, *J. Therm. Anal. Calorim.*, 2016, **125**, 407–421.

71 G. Pieczara, M. Manecki, G. Rzepa, O. Borkiewicz and A. Gaweł, Thermal Stability and Decomposition Products of P-Doped Ferrihydrite, *Materials*, 2020, **13**, 4113.

72 J.-F. Boily and X. Song, Direct identification of reaction sites on ferrihydrite, *Commun. Chem.*, 2020, **3**, 1–8.

73 A. F. Gualtieri and P. Venturelli, In situ study of the goethite-hematite phase transformation by real time synchrotron powder diffraction, *Am. Mineral.*, 1999, **84**, 895–904.

74 A. N. Christensen, T. R. Jensen, C. R. H. Bahl and E. DiMasi, Nano size crystals of goethite, α-FeOOH: Synthesis and thermal transformation, *J. Solid State Chem.*, 2007, **180**, 1431–1435.

75 Y.-H. Chen, Thermal properties of nanocrystalline goethite, magnetite, and maghemite, *J. Alloys Compd.*, 2013, **553**, 194–198.

76 A. P. Roberts, X. Zhao, D. Heslop, A. Abrajevitch, Y.-H. Chen, P. Hu, Z. Jiang, Q. Liu and B. J. Pillans, Hematite (α-Fe_2O_3) quantification in sedimentary magnetism: limitations of existing proxies and ways forward, *Geosci. Lett.*, 2020, **7**, 8.

77 M. Sassi, C. I. Pearce, P. S. Bagus, E. Arenholz and K. M. Rosso, First-Principles Fe L2,3-Edge and O K-Edge XANES and XMCD Spectra for Iron Oxides, *J. Phys. Chem. A*, 2017, **121**, 7613–7618.

78 N. Pinney, J. D. Kubicki, D. S. Middlemiss, C. P. Grey and D. Morgan, Density Functional Theory Study of Ferrihydrite and Related Fe-Oxyhydroxides, *Chem. Mater.*, 2009, **21**, 5727–5742.

